An Empirical Model of the Effects of Ionospheric Electron Density Variations on HF Radar Processing

Marie José Abi Akl[1], Florent Jangal[2], Muriel Darces[3, *], and Marc Hélier[3]

Abstract—The High Frequency hybrid radar mode combines sky and surface wave propagation. As all High Frequency radars, it can be impacted by ionospheric instabilities. A behavioral model able to include ionospheric spatial and temporal variations has been implemented to estimate the impact of ionospheric irregularities on radar signal processing and Doppler-distance images. In this work, probabilistic models of the ionospheric fluctuations in the ray tracing have been introduced using the phase path fluctuation only. Based on Shkarofsky's spectral power density, random variations on some parameters of Booker's electron density profile have been performed to generate disturbed electron density profiles. Afterwards, a propagation delay, integrated in the received radar signal, has been calculated in terms of phase path variation. Moreover, the temporal aspect of the ionospheric variations has been macroscopically implemented by a filtering step according to the Total Electron Content variation. Results of this simulation are presented with the corresponding statistics. Doppler and distance distributions have been computed for several filter cut-off frequency values and for different Shkarofsky's spectral power density parameters. At last, the process described above works properly: its results have been successfully compared with actual radar data for this purpose.

1. INTRODUCTION

For maritime and air surveillance, a High Frequency (HF) hybrid radar mode can be an interesting solution. Basically, this radar mode is a combination of High Frequency Surface Wave Radar (HFSWR) and High Frequency Sky Wave Radar. Despite its over the horizon (OTH) coverage, HFSWR suffers from intrinsic physical limitations. The most penalizing one is the reduced azimuthal coverage about the area to be observed (i.e., often less than 120°). This drawback can be overcome using a mixed sky wave and surface wave OTH deployment: by fixing a frequency between 5 MHz and 12 MHz for HFSWR, coverage from the coast could be ensured to 400 km thanks to the propagation of the waves near the sea surface. On the other hand, by choosing a frequency between 10 MHz and 25 MHz for the sky wave radar, coverage is extended from 400 km to more than 2000 km, thanks to the reflection of the wave on the ionosphere. So, choosing a working frequency between 10 and 12 MHz may lead to a good compromise between both modes of propagation.

Indeed, sky wave OTH radar can launch enough energy to reach maritime targets and surface wave radar can collect the target signals. The main advantage of this sky wave/surface wave association is a continuous coverage combining: a sky wave transmission and surface wave reception for short distance (at low frequencies), or a sky wave transmission and sky wave reception for large distance (at higher frequencies) with, in both cases, a possible scanning over 360° in azimuth, thanks to sky wave antenna arrays.

From user perspectives in an ideal case, a surface wave radar provides a Doppler-distance image as illustrated in Fig. 1(a). Due to the interaction of the surface wave with the sea surface, Bragg's lines are visible. These are two vertical lines, observed near zero Doppler shift. Moreover, a target is also detected at approximately 200 km with a Doppler shift around -0.2 Hz.

Back to the hybrid radar, two types of issues are distinguished depending on its configuration. Firstly, a sky wave transmission and a surface wave reception is considered. Because of a disturbed ionosphere, a Doppler shift and spread are observed on the radar image as shown in Fig. 1(b). The second issue occurs when the transmission is held by surface wave and the reception by sky wave. In this case, non-directive surface wave transmission antennas can cause direct backscatter due to ionospheric irregularities. Consequently, ionospheric clutter appears on the Doppler-distance radar image, as shown in Fig. 1(c). Obviously, the major issue in both cases is due to the ionospheric irregularities that impact on the radar signals. This may result in spread target echos or large target masks depending on the hybrid radar configuration.Therefore, not only ionospheric modeling in the presence of disturbances is important, but also the application of these models to radar processing.

Several models of ionospheric propagation have been elaborated for more than thirty years. For instance, in 1982, Yeh and Liu showed that it is possible to characterize ionospheric irregularities by a power law spectrum applied to the ionospheric electron density [1]. In 1986, Wagen and Yeh proposed a numerical study of waves reflected from a turbulent ionosphere based on the phase screen-diffraction layer method [2]. Zernov and Lundborg have studied in 1995 the influence of electron density fluctuations on the dispersive properties of the ionosphere in the forward scattering approximation by means of a generalized Rytov's method [3]. All these models are based on an accurate description of the involved physical processes. However, they are not suited to the needs of this work, which deal with the estimation of the statistics of radar data corrupted by ionospheric clutter.

Moreover, HF simulator models have been developed to describe ionospheric disturbances effects on communications and trans-horizon radars. For example, HiCIRF (High-Frequency Channel Impulse Response Function) [4] is a model developed to statistically characterize the communication channel. It is a physical model that integrates small-scale variations of the ionosphere considering a received stochastic signal and calculating the ray tracing numerically. Although interesting, this simulator is closed and is not designed to be easily integrated into external radar processing.

As for the application in radar processing, sea clutter has been modeled in previous works to reproduce the Bragg's lines properly [5, 6]. As for sky waves detection, several projects were conducted to find an OTH radar calibration method. The latter were used to study and minimize the influence of natural ionized atmospheric layer. These works are based on the study of the sea clutter and consider short-term ionospheric stability.

The main objective of the work presented in this paper is to complement the radar simulator by the insertion of the ionospheric clutter. In other words, the aim here, as in a former work dealing with sea clutter [5], is to describe the macroscopic behavior of the ionospheric propagation from the radar point of view. To do so, an empirical approach has been adopted which consists in the derivation of the electron density from a Power Spectral Density (PSD) of the electron density relative fluctuation.

To avoid calculation bias due to the insertion of unphysical disturbances and considering especially the continuity of the electron density derivatives, Booker's model has been chosen [7]. Moreover, random Gaussian variations of Booker's parameters result in a log-normal distribution of the electron density as stated by Garner and as observed in several ionospheric experimental characterization campaigns [8]. Thus, the parameters of the synthesized log-normal distributions are in ranges compatible with those of the observed log-normal distributions from the Defense Meteorological Satellite Program [9], depending on latitude, season and hour of the day.

Numerous data have been collected by ONERA under various ionospheric weather in the last decade. In this work the focus will be on identifying the ionospheric phenomena causing poor detection efficiency. The results of simulation as well as the real data will be analyzed from a statistical point of view.
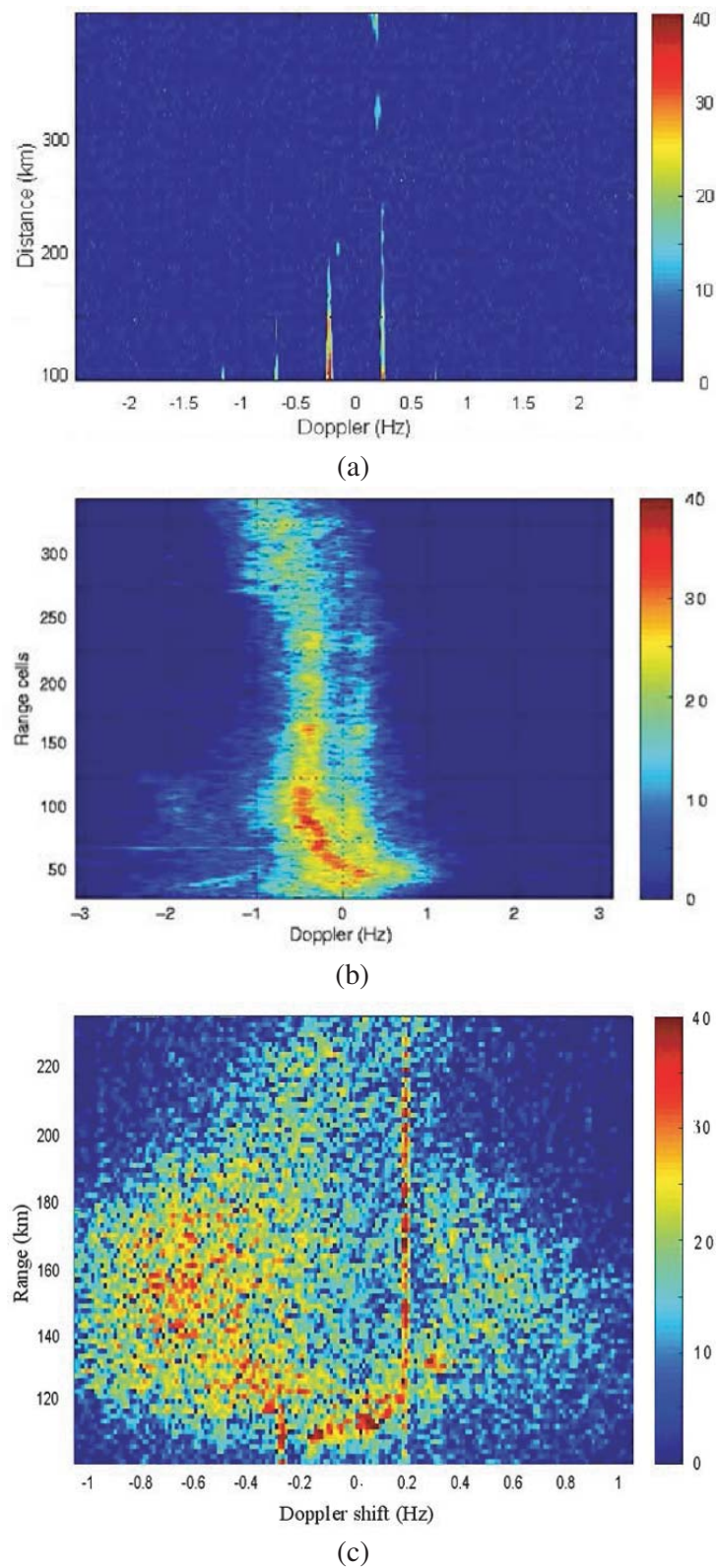
(a)

(b)

(c)

Figure 1. Example of ionospheric irregularities on radar image: (a) Pristine range Doppler image, (b) Doppler shift, (c) ionospheric clutter.

2. BUILDING A STATISTICAL MODEL

The ionosphere is a slowly variable medium in time and space [10]. Apart from the vertical variation of ionization (i.e., the ionization profile), several phenomena are often neglected [11]. For instance, tilts in space as well as diurnal or solar cycle variations in time [12] are not taken into account considering the relatively small Coherent Integration Time (CIT) in maritime surveillance applications. Indeed, the CIT rarely exceeds 180 seconds. Nevertheless, ionization disturbances continuously flow through the ionosphere [13]. Occurring at all altitudes, those disturbances are due to various physical phenomena (gravity waves, solar flare particles, opposite direction particle winds). The actual space and time features of the ionization disturbances give rise to various shapes of clutter in the radar image as shown in Figs. 1(b) and 1(c). From the radar point of view the clutter is characterized by its Doppler spreading and its range spreading.

On the one hand, the Doppler spreading is obviously directly linked to a fluctuation of the phase path during the CIT [14] following:

$$\Delta f_d = -\frac{\omega}{2\pi c_0} \frac{dP(t)}{dt} \tag{1}$$

where Δf_d and $P(t)$ are respectively the Doppler spreading and the phase path during the CIT; ω is the angular frequency; c_0 is the speed of light in vacuum. $P(t)$ is usually obtained using ray tracing as will be explained in the next section.

On the other hand, the range spreading is due to the spatial expansion of the disturbance and is associated with the non-directivity of HF antennas in elevation. In consequence, the ionospheric return echoes are collected from an incident illumination roughly between 5 degrees up to 80 degrees.

Moreover, disturbance fluctuation scan affects both signal from recurrence to recurrence during the CIT and signal in-between Pulse Repetition Interval (PRI). The latter may disturb the range compression and also affect Doppler compression leading to more intricate clutter shape (Fig. 2).
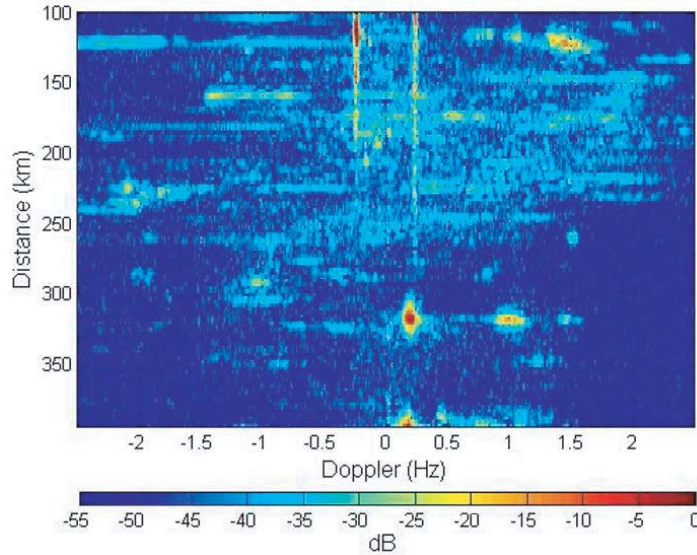

Figure 2. Complex clutter situation measured with Levant Island HFSWR facilities.

In the case of hybrid radar, the OTH radar antenna beam is narrower in elevation than the surface-wave one. Hence the drifts of the disturbances can be observed in the radar image since they affect the apparent Doppler frequency of Bragg lines (Fig. 1(b)).

Considering the unpredictable occurrence of ionosphere disturbances as well as the very large volume of ionosphere illuminated by HF radars (i.e., more than 50 thousand cube kilometers) it is not possible to have real time knowledge of the actual state of the ionosphere. The motivation is to build a behavioral model rendering the statistical aspect of the above mentioned phenomenon. Indeed the used

Constant False Alarm Rate filters for target detection are based on signal statistics. In the following sections we aim to simulate the Doppler spreading due to the refractive index fluctuations inside the disturbance, the range features caused by the antenna directivity in elevation and the disturbance drift. We firstly considered separately those effects. This assumption will be discussed later.

2.1. Building a Behavioral Model

Considering the ionospheric medium as an isotropic medium, basically, the relationship between the refractive index n and the ionospheric electron density N is given by the equation below [15], written with SI units:

$$n = \sqrt{1 - \frac{Ne^2}{4\pi^2\epsilon_0 m f^2}} \tag{2}$$

where e is the electron charge in the electrostatic system, m its mass, ϵ_0 the free space permittivity, and f the working frequency.

From the radar point of view, it is preferable to work with the phase path variations instead of working on the detailed ionization process which includes the actual particles in presence as well as the winds and the motions along the magnetic field [16].

Hence, the well-known relationship between the phase path and the refractive index [14] will be used. In the general case, the phase path $P(t)$ between two points A and B and the ionospheric index n at a z altitude on the ray path, are related as follows:

$$P(t) = \int_A^B n(z,t)\,ds \tag{3}$$

As a consequence, varying N allows to report the variations of the refraction index n, characteristic of the ionospheric disturbances and, hence, to vary the phase path $P(t)$, which will be derived later in the radar process.

The integration involved in Equation (3) is carried out along the ray path supplied here from a 2D ray tracing performed thanks to [12]. $P(t)$ is calculated for each PRI. The ionosphere is assumed to be steady during the PRI (around 20 ms) [17]. This is supposed to be the duration over which the ionosphere is considered constant in time and space. Typically, the temporal variation of the ionospheric profile will be described by the generation of one specific perturbed profile for each PRI. At the end, the phase path obtained varies from one recurrence to another.

Nevertheless, Gherm et al. propose many fluctuation models adequate to rendering the variation of the ionosphere properties in the HF communications frequency bands [18]. From their approach, a disturbed ionospheric profile has been modeled depending on the altitude z. To perform the path calculation, the electron density distribution is given by [2]:

$$N(z) = \langle N_r(z) \rangle + \Delta N_f(z) \tag{4}$$

where $\langle N_r(z) \rangle$ is the regular part of the electron distribution which characterizes the average value of the ionospheric profile, and $\Delta N_f(z)$ is the random part of the electron density fluctuation, which is defined as a random variable. Thus, $N(z)$ is also a random variable. In Section 3, two different ways for deriving $N(z)$ will be proposed.

2.2. HF Hybrid Radar Process

The ionospheric profiles are defined by the electron density that varies with the altitude. Once these profiles are calculated, the ray tracing is applied in order to calculate the phase paths (Equation (3)). The n_θ elevation angles toward which the radar is successively pointed should be specified to complete this step. After that, the delay in the received radar signal is calculated from the phase path. Finally, the radar processing is applied on this signal in order to generate a synthetic radar image, as detailed in the flow chart shown in Fig. 3.

Several parameters need to be identified in order to perform the radar processing. These parameters are listed in Table 1. The radar processing is based on n_{tir} chirp pulses of t_e duration each with a PRI equal to t_r. It is divided into two steps. Firstly, the received signal is handled by applying
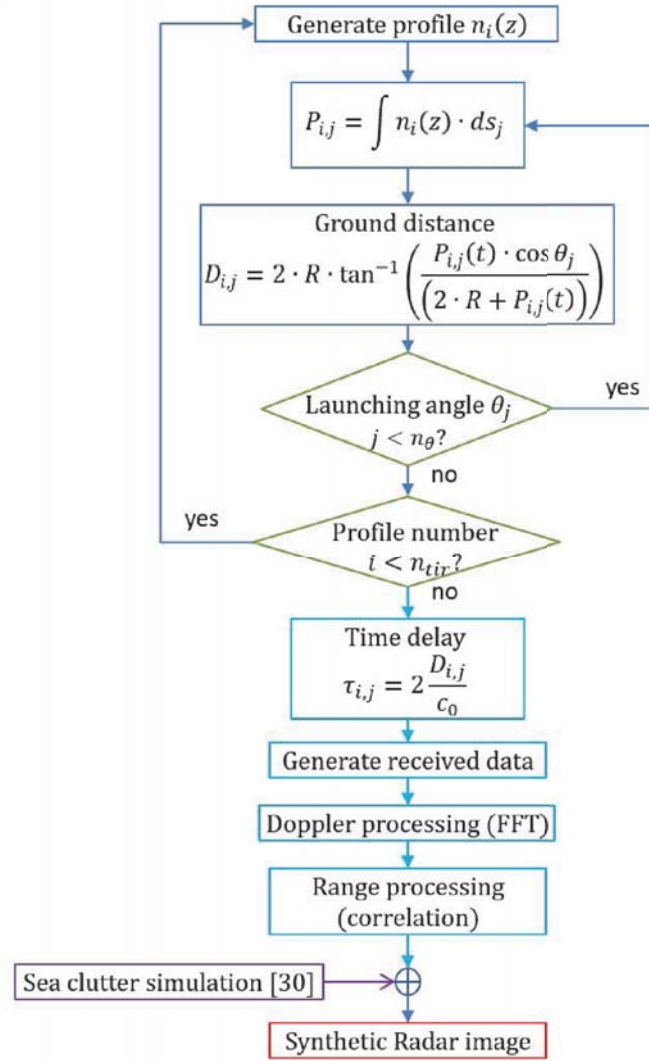
Figure 3. Flow chart detailing the computing of a synthetic HF radar image.

Table 1. Radar process parameters.

n_{tir}	number of recurrences used for the coherent integration
t_r (ms)	recurrence duration equal to the PRI
f_0 (MHz)	carrier frequency
t_e (ms)	transmitting duration
B (kHz)	chirp bandwidth
$n_{tir}.t_r$ (ms)	Coherent Integration Time

a Fourier transform to obtain the Doppler frequencies of targets as well as clutters. The obtained result is correlated then with the transmitted chirp. After this second step, the distance of targets and ionospheric clutter can be known.

In the proposed approach, the ionosphere is assumed to have varied during the CIT, that is to say from one recurrence to the next one. For this purpose, during the CIT, n_{tir} profiles are generated,

namely, one per PRI. As a result, the phase path is fluctuating from recurrence to recurrence which induces random Doppler and distance spreads and shifts.

2.3. Starting Point: Booker's Model

Booker's model has been selected instead of a layered one like the MQP (Multi-Quasi-Parabolic Model) [11], in order to avoid discontinuities while integrating the profiles. Booker's model is based on a global density function which covers the whole altitude range. Moreover, the generated electron density and its derivatives are continuous which avoids adding undesired and non-physical Doppler shifts on radar images due to discontinuities when calculating the ray path.

The ionospheric electron density profile is modeled under the assumption that it follows a combination of exponential variations with respect to the altitude z [7]. Basically, Booker defines three parameters for each inflection point of the electron density profile: the A_i are the slopes of the skeleton profile to the inflection points, the B_i are the reciprocals of the smoothing scales to the inflection points and the z_i are the altitudes of these points. The inflection points are depicted on the profiles in Fig. 4. Applying the formulas given in Equations (5) and (6), the ionospheric electron density profile N will be entirely built from a single continuous function.

$$\log_{10} N(z) = \log_{10} N_0 + A_0(z - z_0) + \sum_{i=1}^{m} (A_i - A_{i-1}) \times [f(z - z_i, B_i) - f(z_0 - z_i, B_i)] \qquad (5)$$

where

$$f(z, B) = B^{-1} ln(1 + e^{Bz}). \qquad (6)$$

N_0 and z_0 are the electron density and altitude of the reference point. $m = 8$ is the number of inflection points needed to draw the skeleton profile, $A_0 = 20 \, cm^{-1}$ and the other reference values are defined in Table 2. The ionospheric profile changes from the day to the night (Fig. 4).

Table 2. Reference values of the parameters of Booker's day profile.

i	1	2	3	4	5	6	7	8
z_i (km)	62.5	82.5	84	100	120	200	250	750
A_i (cm^{-1})	0.1	130	3.125	−1	0.5	2.6	−0.5	−0.05
B_i (km^{-1})	0.5	2	1.5	0.2	0.2	0.16	0.05	0.003

After the generation of Booker's profiles, those will be integrated in the ray tracing. As described above, a discrete sum is performed to calculate the phase path using Equation (3). Therefore, as already explained, having a continuous profile will avoid problems like calculating unrealistic discontinuities while propagating at profile's inflection points.

3. RANDOM PROCESSES APPLIED ON BOOKER'S PROFILE PARAMETERS

In order to randomize the profiles, several variation types have been applied to Booker's profile parameters [19–22]. In this paper, two different approaches have been investigated in order to model the ionospheric fluctuations. In both cases, only one of the four model's parameters A_i, B_i, z_i or N_0 has been randomized. The first approach is based on the generation of random samples of the altitude vector z_i keeping parameters A_i, B_i and N_0 equal to their reference values, as shown in Table 2. The second approach is based on the generation of random samples of the electron density factor N_0. In that case, the vector parameters A_i, B_i and z_i have been kept equal to their values as given by Booker [7].

The reference values have been selected because the resulting profile computed from these parameters is like the one found in the ionosphere under day conditions. It has characteristics like the RRB (Rawer Ramakrishnan Bilitza) profiles [23]. In addition to that, these profiles do not exhibit any discontinuities in derivatives of any order at any height.
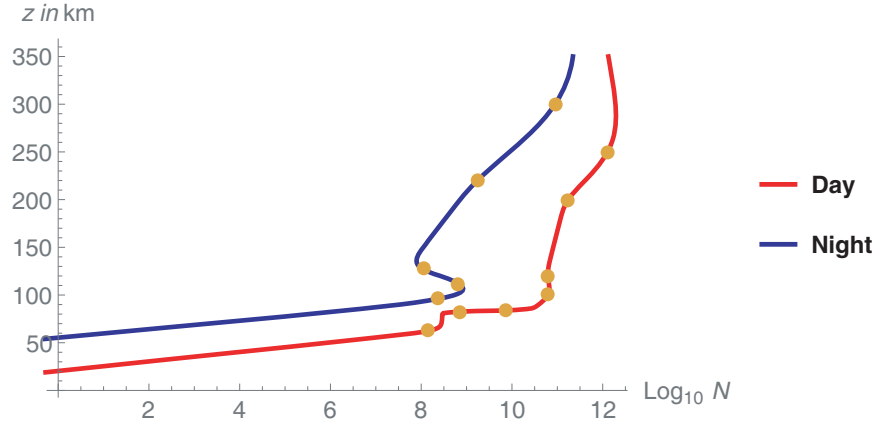
Figure 4. Day and night Booker ionospheric profiles.

3.1. Randomization of Booker's Altitude Parameter z_i

Firstly, the electron density profile is modified by varying the altitude z_i, the other parameters A_i, B_i remaining constant and N_0 equal to $8.51 \times 10^6 \, \mathrm{m}^{-3}$. A sequence of z_i following a multi-normal law built from an exponential correlation function is generated. The probability density function of the random sequence $Z = \{z_i\}$ is defined by Equation (7):

$$e^{-\frac{1}{2}(Z-\{\hat{z}_i\})^T \cdot \Sigma^{-1} \cdot (Z-\{\hat{z}_i\})} \tag{7}$$

where $\{\hat{z}_i\}$ is the mean vector whose components are Booker's height reference values. The covariance matrix $\Sigma = [\Sigma_{pq}]$ ($1 \leq p \leq m$ and $1 \leq q \leq m$) is defined by means of an exponential correlation function as $\Sigma_{pq} = \sigma_z^2 \times e^{(-\alpha|p-q|)}$ with α and σ_z tuned in order to obtain a representative Doppler shift.

The resulting electron density is then governed by a log-normal law [9], at a fixed altitude, as a product of random variables, which has been validated in [8] to be representative of ionospheric fluctuations.

For example, 2048 ionospheric profiles have been computed as shown in Fig. 5(a). The z_i parameters have been varied using the random multi-normal variation which attenuation coefficient is $\alpha = 0.5$ and variance σ_z^2 is equal to $0.01 \, \mathrm{km}^2$. As expected, the electron density histogram at a fixed altitude, 200 km as shown in Fig. 5(b), is governed by a log-normal distribution with three parameters (Johnson's distribution), as described in [9].

Even though randomly varying this parameter fluctuates the ionospheric profiles, this method is discarded because the resulting variations are mostly located at high altitudes. Meanwhile, in the case of HF radars, the reflection occurs at lower altitudes. Moreover, this approach is better justified from a mathematical point of view than a physical one.

3.2. Randomization of N_0, Ionospheric Electron Density at the Reference Altitude z_0

This approach has been applied in order to describe more physically the spatial variation of the ionospheric perturbations. As already explained, the radar coherent processing uses n_{tir} recurrences of t_r duration each, equal to the PRI. Let us call $N_0(it_r) = N_{0,i}$, the discrete value of parameter N_0 during the ith PRI. The procedure applied to generate a sequence of n_{tir} random ionospheric electron density values $N_{0,i}$ starts with the generation of a white noise spectrum. The latter is defined with a unitary amplitude and a randomly varying phase following a uniform probability density function between 0 and 2π [24]. Then, the noise is the input of a transfer function which is proportional to the square root of the generalized Shkarofsky power spectral density of the relative electron density ξ [25], given by Equation (8):

$$PSD(\kappa) = \sigma_N^2 \cdot (\kappa_0 r_0)^{(p-3)/2} \cdot \left(r_0 \sqrt{\kappa^2 + \kappa_0^2}\right)^{-p/2} \cdot \frac{K_{p/2}\left(r_0 \sqrt{\kappa^2 + \kappa_0^2}\right) \cdot r_0^3 \cdot (2\pi)^{3/2}}{K_{(p-3)/2}(\kappa_0 r_0)} \tag{8}$$
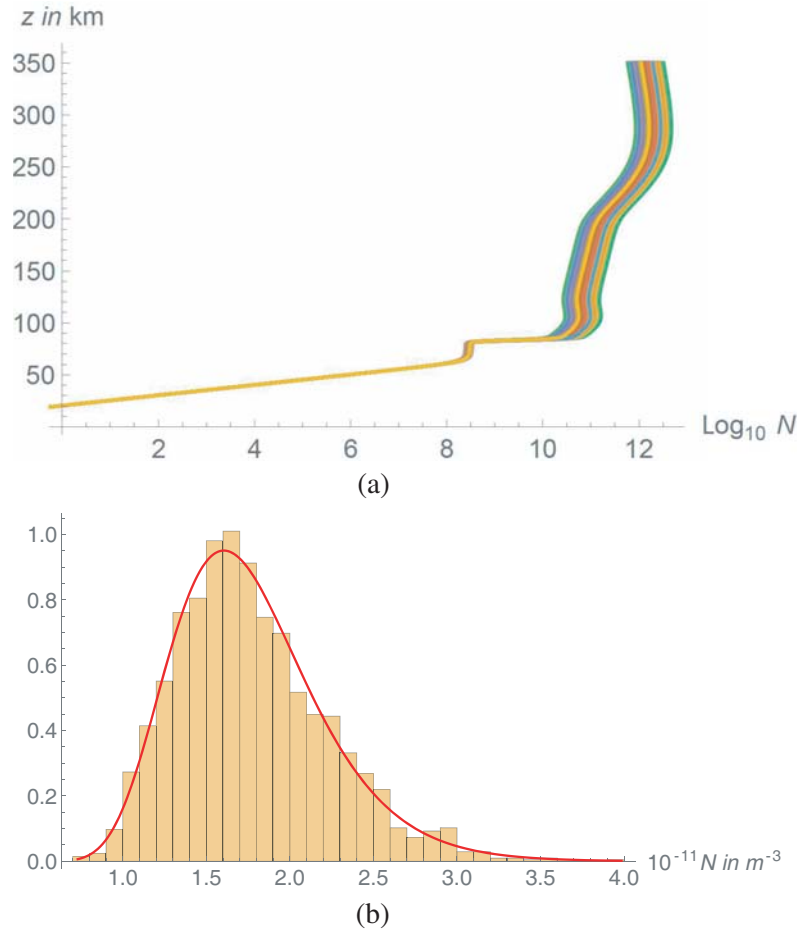
(a)

(b)

Figure 5. Example of perturbations generated by randomizing the z_i at the inflection points: (a) Disturbed ionospheric profiles, (b) cut at $z = 200$ km of the ionospheric electron density log-normal distribution for corresponding disturbed profiles.

p is the spectral index, $\sigma_N^2 = \langle \xi^2 \rangle$ is the variance of the relative electron density fluctuation, κ is the spatial wave number and K_s is the Bessel-Kelvin function of order s. $\kappa_0 = 1/l_0$ with l_0 being the outer scale and r_0 the inner scale of the ionospheric disturbance.

ΔN_0 is referred as the variation of the reference electron density and $\langle N_0 \rangle$ its mean value. Then, the electron density relative variation $\Delta N_0 / \langle N_0 \rangle$ is calculated by applying an inverse Fourier transform to the product of the previous white noise by the transfer function previously defined [26]. The first step of the disturbed profile generation procedure is schematized in Fig. 6. The spatial aspect and temporal processing are described in the next section.
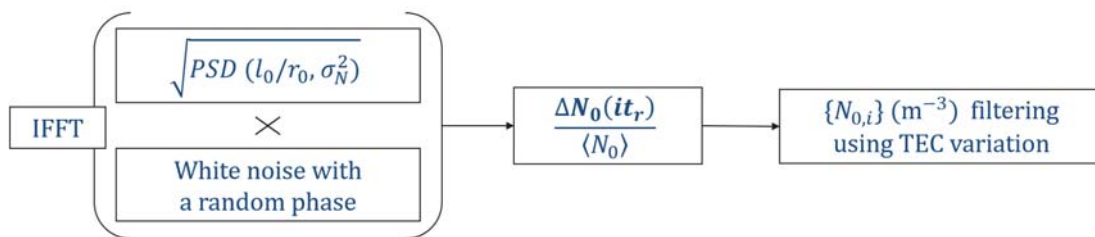

Figure 6. Spatial and temporal distribution of N_0 due to a power spectral density function.

In consequence, the corresponding fluctuating part ϵ_1 of the dielectric permittivity is given by [1, 27]:

$$\epsilon_1 = \xi\beta; \qquad \xi = \frac{\Delta N_0}{\langle N_0 \rangle}; \qquad \beta = \frac{\omega_p^2}{\omega^2 - \omega_p^2} \qquad (9)$$

where ω_p is the circular plasma frequency.

3.3. Applying a Low-Pass Filter

In the chosen approach, the profiles are randomly generated at each PRI. That can result in large phase path variations and then gives rise, after the Doppler processing, to huge and unrealistic Doppler shifts due to excessive path variations during the CIT. Hence a limitation in the rate of change of the electron concentration is needed. A way to achieve that is to apply a finite impulse response low-pass filter to the n_{tir}-length sequence of $N_{0,i}$ in order to reproduce the bounded temporal aspect of the ionospheric variation. Its cutoff frequency has been defined from papers [25, 28], dealing with the TEC (Total Electron Content) measurements [29] and assuming that TEC's rate of change is linked to those of the ionospheric electron density. Following this way, realistic Doppler shifts and distance spreads have been obtained on radar images.

That filter has been implemented using built-in Mathematica® functions which optimized the filter kernel length and the coefficients of a finite impulse response filter after the prior application of a Hamming window and tries to approach them as close as possible to the ideal response by the least squares method. The generation of random profiles is also implemented in Mathematica® with tailored functions.

4. HF CLUTTER SIMULATOR RESULTS

The final clutter simulator model is based on the generation of ionospheric profiles disturbed by means of the electron density power spectral density at the reference altitude z_0. In fact, the PSD applied in this approach describes more physically the fluctuation that is randomly added to disturb the ionospheric profiles than the fine tuned variation of Booker's skeleton altitude z_i. Moreover, the chosen PSD for the variation of z_0 is linked to the physical dimensions of fluctuation with an overall variation adjustable via σ_N^2.

In the next section, full clutter simulation results will be presented firstly in order to illustrate the images obtained with the proposed approach. Furthermore, the time needed to compute such images as well will be provided. Moreover, a synthetic image will be compared, notably in terms of statistics, to an actual radar image obtained from actual measured data. And finally, the influence of the power spectral density parameters on the Doppler and distance spreads will be discussed.

4.1. Full Clutter Simulation Example

Different combinations of the parameters were used in the PSD and Booker's functions. The first synthetic image shown has been computed using the following parameters: $l_0 = 7\,\text{km}$, $r_0 = 5\,\text{m}$, $p = 11/3$ and $\sigma_N^2 = 10^{-2}$.

In fact, in order to have a better range spreading on the radar image, the dimension l_0 is slightly bigger than the one used before. The cutoff frequency of the TEC-inspired filter is set to $0.07\,\text{Hz}$ in order to avoid unrealistic or folded Doppler spread. The resulting radar image is shown in Fig. 7. This image shows the simulated ionospheric clutter observed when covering the ionospheric clutter from 45 to 80 degrees in elevation with a step of 0.1 degree representing the lack of directivity of the antennas in elevation. The altitude of the reflection is near $100\,\text{km}$ corresponding to a disturbance in the classical F1 layer. It leads to a clutter located in distance between $80\,\text{km}$ and $250\,\text{km}$.

The obtained clutter spreading depends on the ionospheric profiles and on the drift velocity of the generated ionospheric irregularity. The clutter spreading observed on this radar image can be compared to the one observed on a real radar image shown in Fig. 1(c). The clutter represented in Fig. 7 is slightly drifting, therefore the Doppler shift is barely negative. In fact, in both images, the clutter spreads, approximately, along $120\,\text{km}$ in distance and $1\,\text{Hz}$ in Doppler. Moreover, it is obvious that
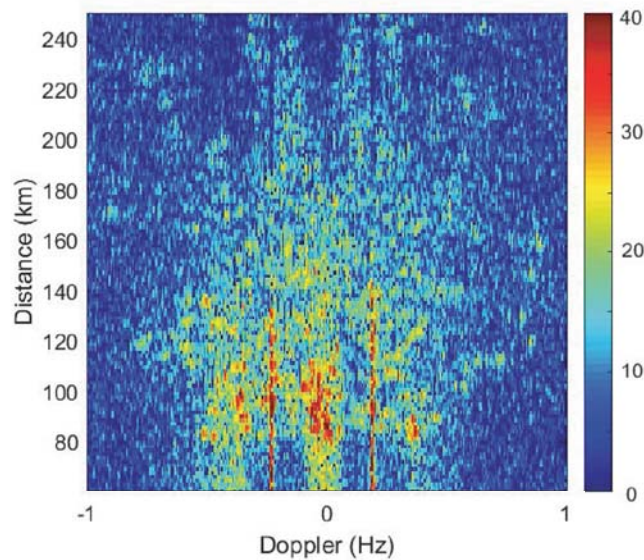
Figure 7. Synthetic image of the ionospheric clutter for elevation angles between 45 and 80 degrees.

the clutter shown on the real image is drifting faster than the simulated one. Therefore, the clutter represented in Fig. 7 has a Doppler shift almost centered around zero contrariwise to that in Fig. 1(c) where the Doppler shift is mainly negative. On the other hand, no clutter is observed below 60 km because this distance range corresponds to the radar blind zone, which is the distance equivalent to the time needed for the transmission of the first chirp.

Furthermore, the time needed to obtain that image with Matlab is about 35 hours, generating 400 angles between 45 and 80 degrees. The simulation has been run on a "Macintosh computer under Mac OS X version 10.6.8, with a 2.8 GHz Intel Core i7 processor, and 16 Go 1067 MHz DDR3 memory". This duration includes saving data files for 400 angles, with 2048 profiles generated for each angle.

The two vertical lines observed near Doppler zero are Bragg's lines. In the approach described in this paper, those lines are integrated as a template without any computation, in order to render a realistic radar image. Besides the generation of these lines has been performed in this example for a radar frequency of 7 MHz, a wind speed of 4 m/s and a wind-radar angle of 45 degrees. They are inserted as a vector of values on the simulated image. However the template is not to be compared to the Bragg's line figured in the real radar image case. In future work, a full HF radar simulator will be implemented to generate on the same radar image both physical ionospheric and sea clutter.

4.2. Statistical Comparison of Actual and Synthetic Radar Image

To perform this second comparison, a synthetic radar image was generated and compared to a real radar image acquired in similar conditions. In order to reduce the time of computation, an actual radar image with two meteor trail style clutter was chosen, as shown in Fig. 8(a). The measurements are carried out at a frequency of 7 MHz and a PRI equal to 10 ms. Sea clutter and ionospheric disturbance are shown in this radar image: the clutter between Bragg's lines is the sea clutter.

As mentioned before, two ionospheric clutter trails due to ionospheric disturbances are identified in the upper third of the actual radar image. These disturbances are approximately located at distances of 500 km and 600 km, respectively. Statistics has been calculated over these two spots separately: the upper clutter, near 600 km has a Doppler standard deviation of 0.41 Hz and a distance standard deviation of 6.9 km. The clutter at 500 km has a Doppler standard deviation of 0.47 Hz and a distance one of 4.9 km.

As there are only two single significant ionospheric clutter returns, using only two corresponding angles of elevation is enough. This choice is made in order to reduce the calculation time. The elevation
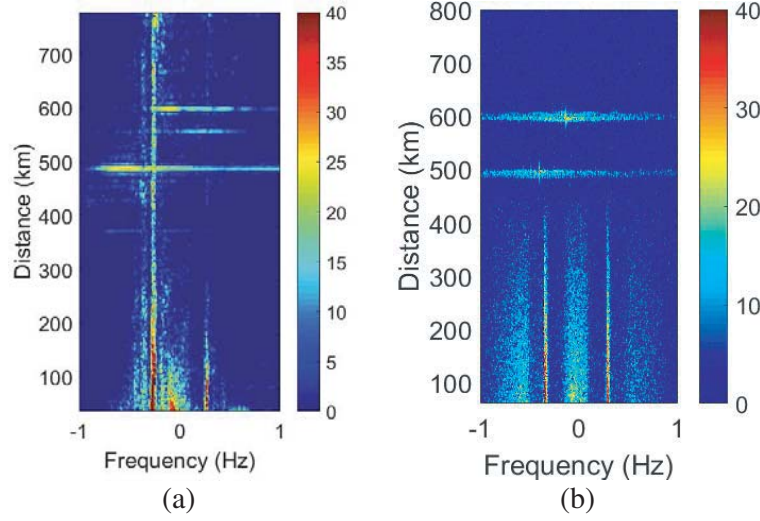
Figure 8. Comparison between a real radar image and a synthetic one involving two distinct ionospheric perturbations: (a) Actual radar image, (b) synthetic radar image.

angles were chosen in a way to have two disturbed spots located at the same positions of those on the real radar image of Fig. 8(a).

Moreover, initial conditions of the radar processing in this HF simulator were set exactly like the values of those used by the actual radar, as listed in Table 3. The radar CIT is equal to 40.96 s which corresponds to 4096 recurrences with a PRI equal to 10 ms. At this step, 4096 random ionospheric profiles were generated considering that the ionospheric coherent time is equal to the recurrence duration (10 ms). As a result, 4096 phase paths have been calculated when proceeding via ray tracing. Further, Martyn's theorem [30] is applied to calculate the ground distance. At last, the ground distances are added as a time delay in the received radar signal in order to draw the radar image.

Table 3. Parameters to generate a synthetic radar image with statistical properties similar to those of the actual one.

Radar process parameters		PSD parameters	
n_{tir}	4096	σ_N^2	10^{-2}
t_r (ms)	10	p	11/3
t_e (ms)	0.5	l_0 (m)	5000
f_0 (MHz)	7	r_0 (m)	5
B (kHz)	50		

Furthermore, to apply the method based on the generation of parameter N_0 from the power spectral density, Booker's reference values were fixed to the day's ones in order to compute the electron density. The undisturbed resulting profile is drawn in Fig. 4. In order to randomize that profile, the chosen parameters for the spectral power density $PSD(\kappa)$ are: $\sigma_N^2 = 10^{-2}$, $p = 11/3$ and $l_0/r_0 = 1000$ (supposing $l_0 = 5\,\text{km}$) [28].

To summarize, the back-scattering of the ionosphere has been studied at 7 MHz from two different ionospheric irregularities, located at elevation angles of $20°$ and $25°$, respectively. Knowing that no target is detected on the actual radar image, it can be concluded from the Doppler signature that these irregularities drift, respectively, at an apparent radial velocity of 2 m/s (Doppler frequency = −0.13 Hz) and of 6 m/s (Doppler frequency = −0.4 Hz). The low-pass filter cutoff frequency has been set to 1 Hz [29]. The corresponding parameters used to generate this synthetic radar image are listed in Table 3 resulting in a larger Doppler spreading. The simulated radar image obtained is displayed in Fig. 8(b).

It should be reminded that such radar images result from random processes and that they can be considered as random draws. So it would be highly improbable to have a perfect matching between two radar images (simulated or measured) computed from the same random model. However, these images can be compared in terms of their statistical properties.

A statistic analysis of the Doppler and distance spreads has been performed for both ionospheric irregularities in the synthetic radar image case. These results are shown in Fig. 9. Specifically, for the disturbance drifting with an apparent radial velocity of $6\,\mathrm{m/s}$, the Doppler distribution has a standard deviation $\sigma = 0.3\,\mathrm{Hz}$ and a mean $\mu = -0.24\,\mathrm{Hz}$ and the distance distribution is characterized by $\sigma = 4\,\mathrm{km}$ and $\mu = 493\,\mathrm{km}$. Furthermore, for the ionospheric perturbation drifting with an apparent radial velocity of $2\,\mathrm{m/s}$, the Doppler distribution has a standard deviation $\sigma = 0.4\,\mathrm{Hz}$ and a mean $\mu = -0.15\,\mathrm{Hz}$, and for the distance distribution $\sigma = 5\,\mathrm{km}$ and $\mu = 597\,\mathrm{km}$.
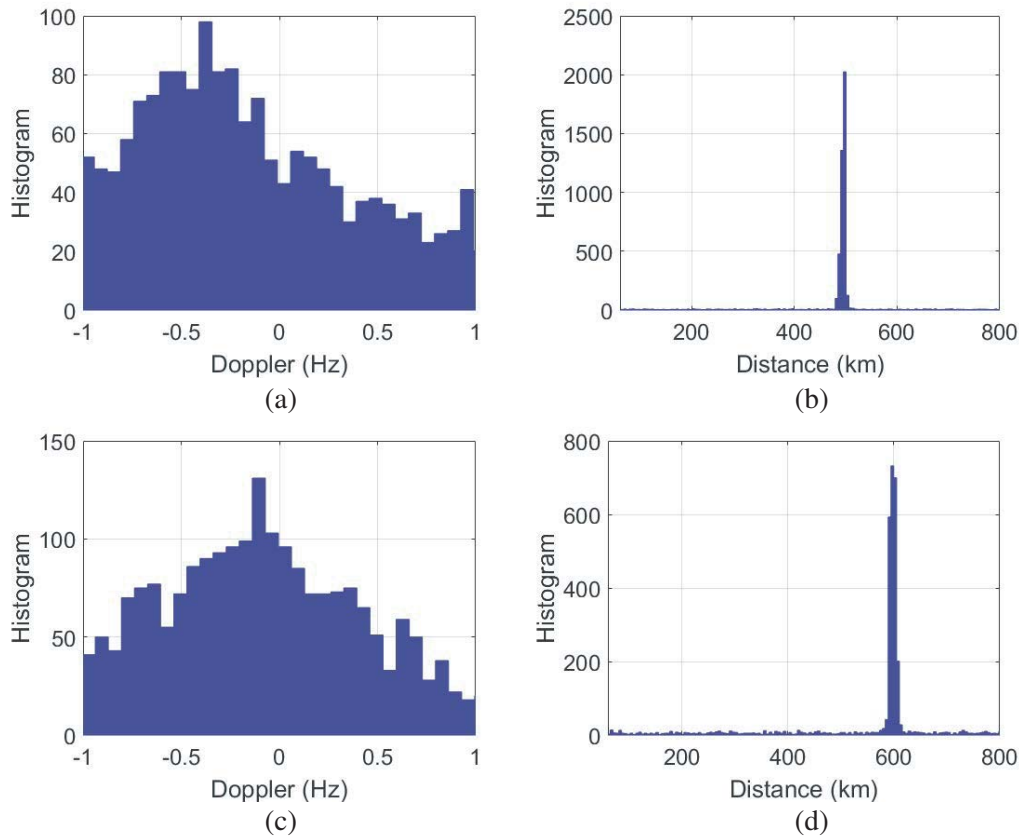

Figure 9. Effects of a drifting ionospheric disturbance located at two elevation angles of $25°$ and $25°$ respectively: (a), (b) Doppler and distance distribution for an apparent radial speed of $6\,\mathrm{m/s}$, (c), (d) Doppler and distance distribution for an apparent radial speed of $2\,\mathrm{m/s}$.

The statistical properties of the synthetic image are close to those obtained from real radar measurements with a maximum difference of 27% in terms of Doppler and distance spreads. It should be noted that the parameters of the actual irregularities are not known and that the parameters of the synthetic irregularities could be improved, in future works, by means of an optimization approach.

In the next sections, statistics on the radar image will be presented when varying the parameters of the $PSD(\kappa)$ and the filter cutoff frequency f_{TEC}.

4.3. Sensitivity to the Variation of the Power Spectral Density Parameters

As explained before, the starting point was a power spectral density trimmed with three main parameters in order to generate a disturbed ionospheric electron density (8): the relative electron density fluctuation

variance σ_N^2, the fluctuation scale ratio l_0/r_0 and the spectral index p. In this section, the impact of these parameters, as observed on the synthetic radar image, will be analyzed in terms of Doppler and distance spreads through their standard deviations.

4.3.1. Electron Density Fluctuation Variance Variation

At first, the impact of the σ_N^2 parameter on radar processing will be studied, assuming that the ionospheric disturbance dimensions remain constant during the radar processing. The variation of Doppler and distance standard deviations due to σ_N^2 is plotted in Fig. 10. The ionospheric disturbance dimension is fixed to $l_0/r_0 = 1000$ such as $r_0 = 5\,\text{m}$. The spectral index p is equal to $11/3$. For the radar processing, the transmission time has been set to $t_e = 1\,\text{ms}$ and the reception time to $t_r = 25\,\text{ms}$.

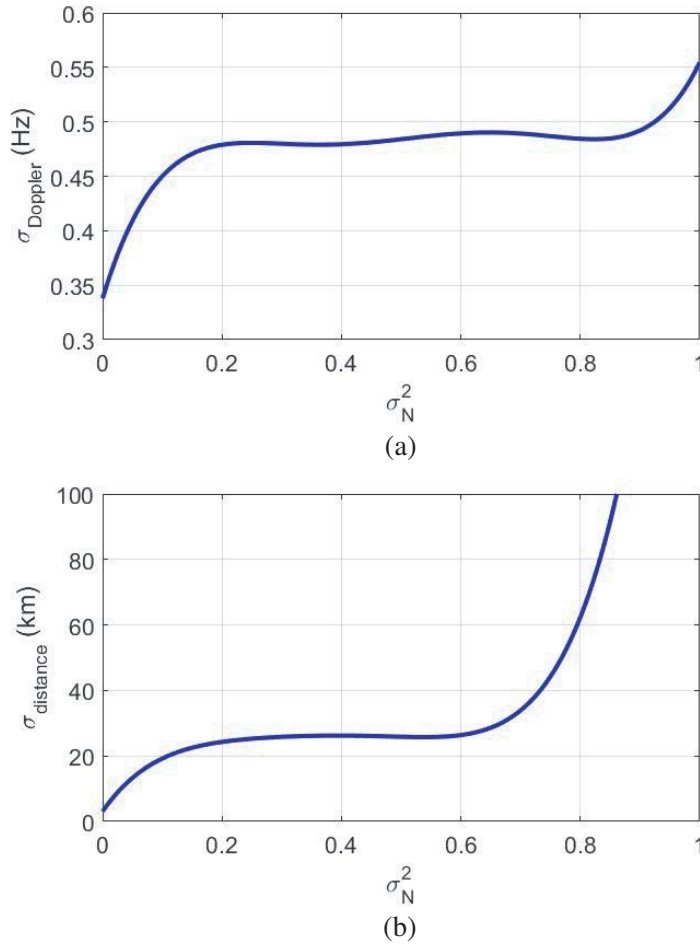**Figure 10.** σ_N^2 sensitivity on synthetic radar image: (a) Variation of the Doppler standard deviation, (b) variation of the distance standard deviation.

It can be seen that the σ_N^2 parameter has similar impacts on the Doppler and the distance standard deviations. As a matter of fact, when increasing σ_N^2, the Doppler and distance standard deviations increase as well, and conversely with decreasing σ_N^2. This result sounds plausible, since the fluctuations of electronic density become stronger with the growth of the variance σ_N^2. However, the standard deviations of the Doppler shift and the distance seem more sensitive to low values of the electron density variance. On the other hand, for values of σ_N^2 close to 1, the Doppler and distance standard deviations increase rapidly. In this case, the gap between the profiles becomes very large, which leads to a large spread of the phase path values.

4.3.2. Spectral Index Variation

In this case, σ_N^2 variance and l_0/r_0 ratio are set to 10^{-2} and 1000, respectively. The standard deviations of the Doppler and the distance spreads are shown in Fig. 11.
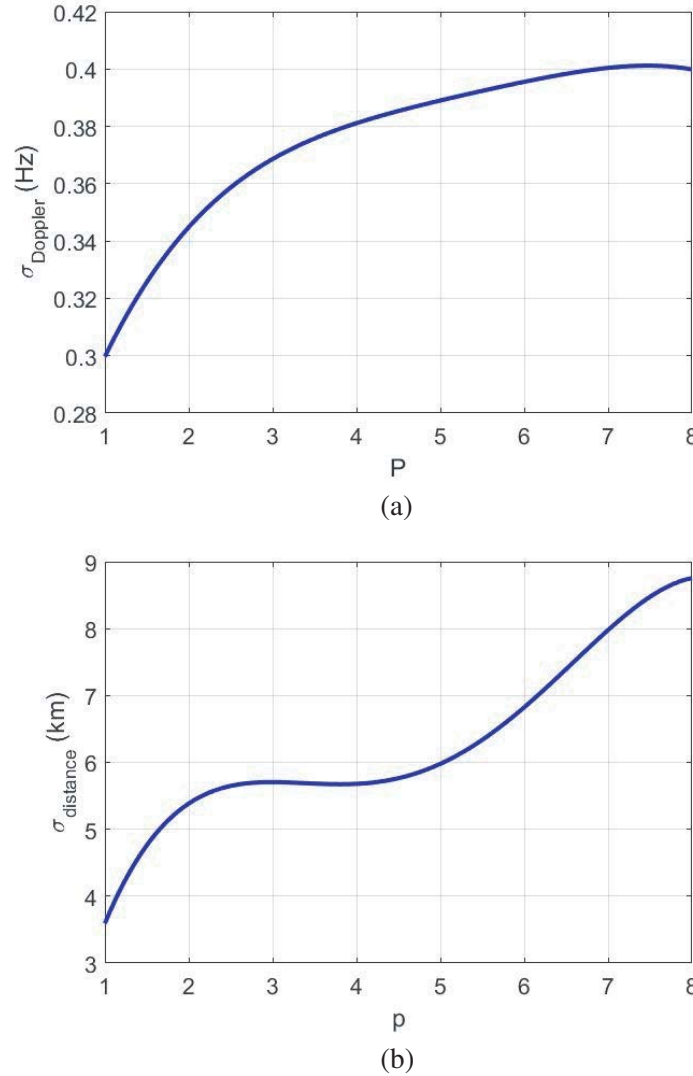

(a)

(b)

Figure 11. p sensitivity on synthetic radar image: (a) Variation of the Doppler standard deviation, (b) variation of the distance standard deviation.

The spectral index variation introduces less dispersion over the distance than the dispersion observed in the case of the variation of σ_N^2. Classically, the spectral index p takes values between 1.4 and 4.8 [28]. In Fig. 11, a weak Doppler and distance standard deviation variations (0.05 Hz and 2 km) have been observed associated to that range of p.

4.3.3. Ionospheric Clutter Dimension Variation

The ionospheric clutter dimension is defined through two parameters, the inner scale parameter r_0 and the outer scale parameter l_0. Here, the inner scale is fixed to 5 meters, and the outer scale is varying. The ionospheric power spectral density variance is fixed to $\sigma_N^2 = 10^{-2}$ and the spectral index to $p = 11/3$. The resulting Doppler and distance standard deviations computed from the synthetic radar image are shown in Fig. 12.
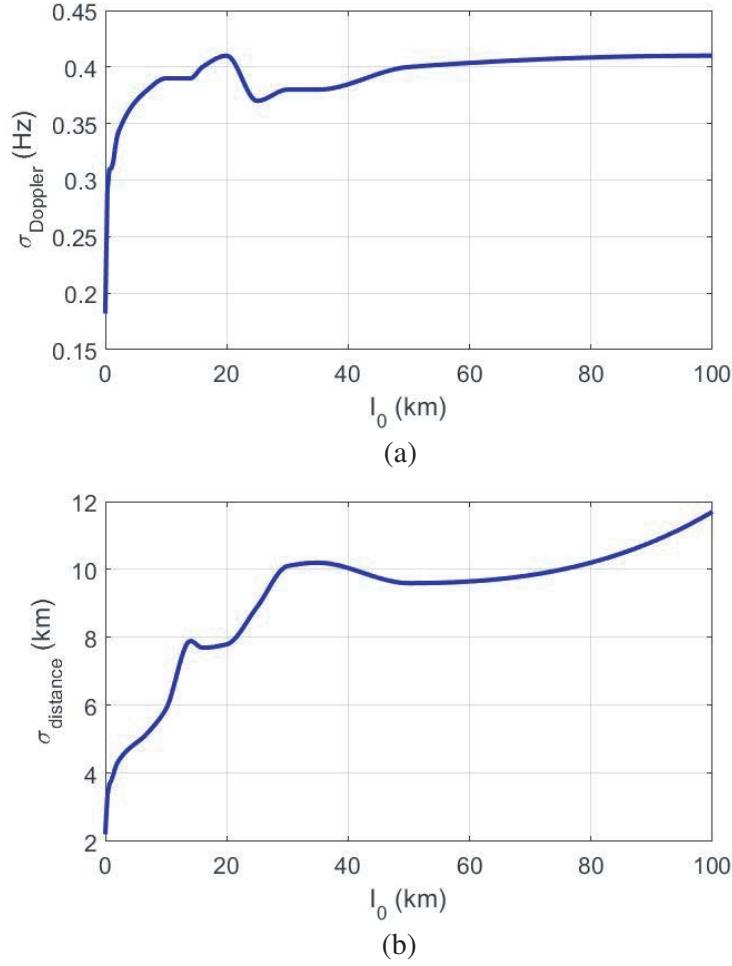
Figure 12. l_0 sensitivity on synthetic radar image: (a) Variation of the Doppler standard deviation, (b) variation of the distance standard deviation.

The variation of the l_0 dimension of the disturbance ranges from a few meters to 100 kilometers. Fig. 12(a) shows the variation of the Doppler shift standard deviation as a function of l_0. The standard deviation rapidly increases with the dimension of the disturbance. The standard deviation reaches a maximum of 0.41 Hz for $l_0/r_0 = 20$. Beyond this value, Doppler standard deviation remains constant. This may be due to the fact that, for a very large irregularity, the perturbation tends to be mislocated by the radar due to range migration.

Moreover, poor compression will occur at the radar processing level. This weakens the amplitude of the signal and it will be mistaken for the noise. Then, the detection will be erroneous on the synthetic radar image.

In conclusion, by varying the parameters of the power spectral density function PSD, especially l_0 and σ_N^2, a wide variety of clutter types with various smears in distance or Doppler can be accounted.

4.4. Effects of the Low-pass Filter

The low-pass filter processing is necessary to bound the rate of change of the electron density. The filter cutoff frequency reflects the frequency behavior observed in the TEC measurements. It has different impacts on the generation of disturbed profiles as it is the case with the parameters of the power spectral density. As in the previous cases, the power spectral density function is applied to generate the spatial disturbed profiles. Fig. 13 and Fig. 14 illustrate the variation of the electron density for different cutoff
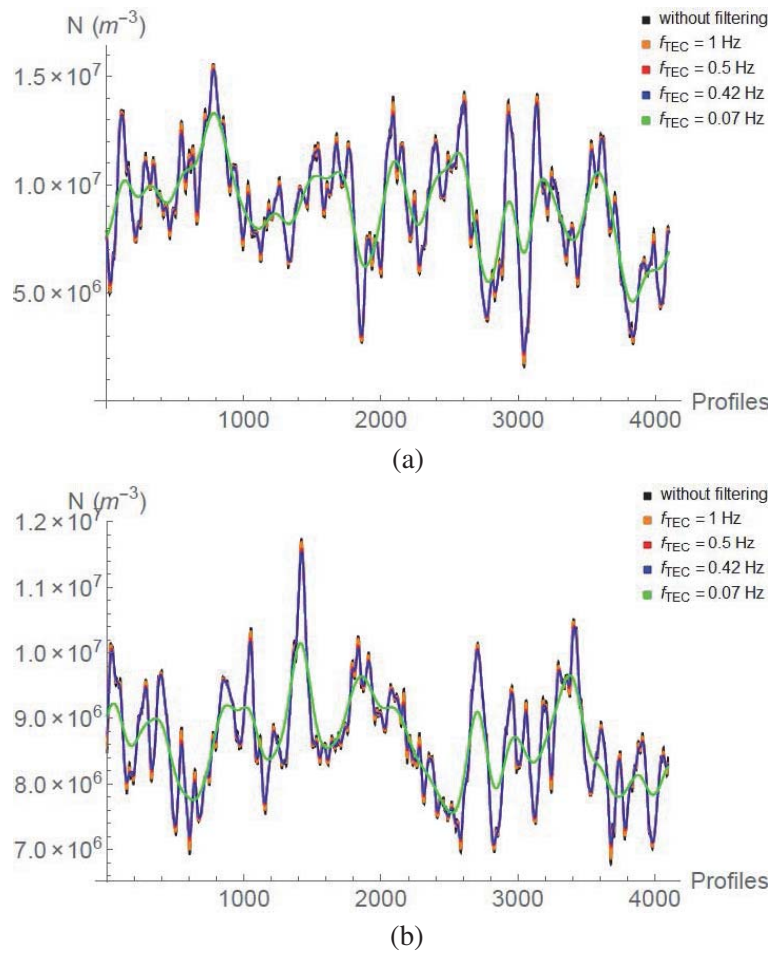
Figure 13. Filtering effects on the ionospheric electron density N when varying the $PSD(k)$ as following: (a) $l_0 = 5\,\text{km}$ and $\sigma_N^2 = 0.1$, (b) $l_0 = 5\,\text{km}$ and $\sigma_N^2 = 0.01$.

frequencies. Figs. 13(a) and 13(b) concern a clutter dimension $l_0 = 5\,\text{km}$ with a relative electron density fluctuation variance $\sigma_N^2 = 0.1$ and $\sigma_N^2 = 0.01$ respectively. Figs. 14(a) and 14(b) refer respectively to the same relative electron density fluctuation variance σ_N^2 with a clutter dimension $l_0 = 50\,\text{km}$. For the chosen σ_N^2 values, the Doppler and distance spreads vary significantly.

The figures show the reference electronic density generated and filtered for different cutoff frequencies. The cutoff frequencies applied are: 1 Hz (orange), 0.5 Hz (red), 0.42 Hz (blue) and 0.07 Hz (green). Based on the literature, the minimum value of the cutoff frequency is 0.07 Hz. The black curve represents the values of N without processing by the low-pass filter.

The results shown in these curves depend on two parameters. First, l_0 is fixed and the variation of N is studied. The latter decreased as the value of the cutoff frequency lowers. Then, when fixing σ_N^2 and in order to observe a filtering effect, l_0 should increase when the cutoff frequency of the filter becomes smaller.

To conclude, the low-pass filter serves to limit the rate of temporal variation between successive random draws of the profiles. The effect of this filtering varies not only as function of the chosen cutoff frequency but also as a function of the parameters of the spectrum power density of the synthesized disturbance. When the size of the disturbance is large, the low-pass filter has little influence.
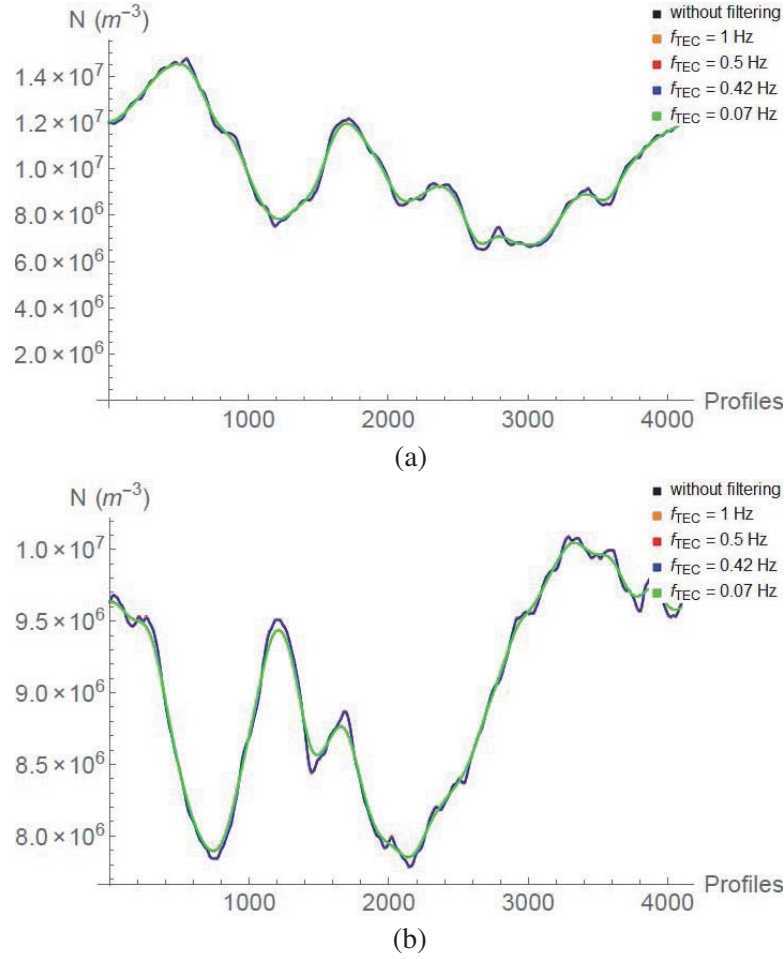
Figure 14. Filtering effects on the ionospheric electron density N when varying the $PSD(k)$ as following: (a) $l_0 = 50\,\text{km}$ and $\sigma_N^2 = 0.1$, (b) $l_0 = 50\,\text{km}$ and $\sigma_N^2 = 0.01$.

5. CONCLUSION

Radar images are highly disturbed by the wave propagation through a disturbed ionosphere. In this study, an HF simulator has been designed to render different types of ionospheric clutter. The study is based on the ionospheric behavior and the evolution in time and space of the electron density. The most satisfactory approach developed is based on the variation of the reference ionospheric electron density.

The resulting random ionospheric profiles have been generated spatially by means of the power spectral density function of Shkarofsky [25]. Then, the temporal variation boundary has been implemented using data known from TEC measurements. Those data have been analyzed in order to define a low-pass filter to be applied on the ionospheric electron density.

Final results have been compared with actual radar data measured in the Onera "Radar Basse Frequence" group, which is interested in the study of the detection of maritime and aeronautical targets using HF radars. These results are very promising and illustrate satisfactory performances of the HF clutter simulator. Finally, corresponding statistics mean and standard deviation of synthesized ionospheric disturbances have been computed over a large amount of data, capable to describe different types of clutter evolution and their impacts on the Doppler and the distance spreads.

Even if the chosen approach still has some limitations as it is a behavioral one, it is very versatile since numerous sizes of irregularities as well as rate of fluctuations can be simulated.

The next step will be to enhance that approach by 3D ray tracing, taking thus into account the magnetic field, before implementing it in a full HF radar simulator.

REFERENCES

1. Yeh, K. C. and C.-H. Liu, "Radio wave scintillations in the ionosphere," *Proceedings of the IEEE*, Vol. 70, No. 4, 324–360, April 1982.

2. Wagen, J.-F. and K. C. Yeh, "A numerical study of waves reflected from a turbulent ionosphere," *Radio Science*, Vol. 21, No. 4, 583–604, July–August 1986.

3. Zernov, N. N. and B. Lundborg, "The influence of ionospheric electron density fluctuations on HF pulse propagation," *Journal of Atmospheric and Terrestrial Physics*, Vol. 57, No. 1, 65–73, 1995.

4. Nickisch, L. J., G. St. John, S. V. Fridman, M. A Hausman, and C. J. Coleman, "HiCIRF: A high-fidelity HF channel simulation," *Radio Science*, Vol. 47, No. 4, RS0L11, 2012.

5. Jangal, F., P. Dorey, M. Menelle, and N. Bourey, "HF radars and HF propagation simulations," *2013 7th European Conference on Antennas and Propagation (EuCAP)*, 2692–2693, April 2013.

6. Halim, R. A. and M. D. Seck, "The simulation-based multi-objective evolutionary optimization (SIMEON) framework," *Proceedings of the 2011 Winter Simulation Conference (WSC)*, 2834–2846, Phoenix, AZ, USA, December 2011.

7. Booker, H. G., "Fitting of multi-region ionospheric profiles of electron density by a single analytic function of height," *Journal of Atmospheric and Terrestrial Physics*, Vol. 39, No. 5, 619–623, 1977.

8. Garner, T. W., B. T. Taylor, T. L. Gaussiran, W. R. Coley, and M. R. Hairston, "On the distribution of ionospheric electron density observations," *Space Weather*, Vol. 3, No. 10, 2005.

9. Garner, T. W., B. T. Taylor, T. L. Gaussiran, W. R. Coley, M. R. Hairston, and F. J. Rich, "Statistical behavior of the topside electron density as determined from DMSP observations: A probabilistic climatology," *Journal of Geophysical Research: Space Physics*, Vol. 115, No. A7, 2010.

10. Yeh, K. C. and C. H. Liu, *Theory of Ionospheric Waves*, Academic Press, 1972.

11. Robinson, I. and P. L. Dyson, "Effects of ionospheric irregularities on radio waves — I. Phase path changes," *Journal of Atmospheric and Terrestrial Physics*, Vol. 37, No. 11, 1459–1467, 1975.

12. Dyson, P. L. and J. A. Bennett, "A model of the vertical distribution of the electron concentration in the ionosphere and its application to oblique propagation studies," *Journal of Atmospheric and Terrestrial Physics*, Vol. 50, 251–262, March 1988.

13. Fejer, B. G. and M. C. Kelley, "Ionospheric irregularities," *Reviews of Geophysics and Space Physics*, Vol. 18, 401–454, May 1980.

14. Dyson, P. L., "Relationships between the rate of change of phase path/Doppler shift/and angle of arrival," *Journal of Atmospheric and Terrestrial Physics*, Vol. 37, 1151–1154, August 1975.

15. Jouaust, R., "L'ionosphère et les évanouissements brusques des ondes radioélecriques courtes," *J. Phys. Radium*, Vol. 10, No. 6, 251–259, 1939.

16. Snyder, W. and R. A. Helliwell, "Universal wave polarization chart for the magneto-ionic theory," *Journal of Geophysical Research*, Vol. 57, No. 1, 73–84, 1952.

17. Hanuise, C., J. P. Villain, D. Gresillon, B. Cabrit, R. A. Greenwald, and K. B. Bakerl, "Interpretation Of HF radar ionospheric Doppler spectra by collective wave scattering-theory," *Annales Geophysicae*, Vol. 11, No. 1, 29–39, 1993.

18. Gherm, V. E., N. N. Zernov, H. J. Strangeways, and M. Darnell, "Scattering functions for wideband HF channels," *2000 Eighth International Conference on HF Radio Systems and Techniques*, 341–345, Guildford, UK, July 2000.

19. AbiAkl, M. J., F. Jangal, M. Darces, and M. Hélier, "Behavioral model of ionospheric effects in HF radars," *2017 11th European Conference on Antennas and Propagation (EUCAP)*, 1254–1257, Paris, France, March 2017.

20. AbiAkl, M. J., F. Jangal, M. Darces, and M. Hélier, "Modelling the ionospheric effects in HF radar long term integration," *2016 10th European Conference on Antennas and Propagation (EuCAP)*, 1–4, Davos, Switzerland, April 2016.

21. AbiAkl, M. J., F. Jangal, M. Darces, and M. Hélier, "Modèle comportemental pour radars HF d'une ionosphère perturbée," *Conference JNM 2017, 20èmes Journées Nationales Micro-Ondes*, Saint-Malo, France, May 2017.

22. AbiAkl, M. J., F. Jangal, M. Darces, and M. Hélier, "Ionospheric clutter simulator for high frequency radars wave propagation," *Conference IEEE APS/URSI 2017, IEEE International Symposium on Antennas and Propagation and USNC-URSI Radio Science Meeting*, San Diego, United States, July 2017.

23. Rawer, K., D. Bilitza, and S. Ramakrishnan, "Goals and status of the international reference ionosphere," *Reviews of Geophysics*, Vol. 16, No. 2, 177–181, 1978.

24. Gavin, H. P., "Random processes, correlation, and power spectral density," Duke University, 2016.

25. Shkarofsky, I. P., "Generalized turbulence space-correlation and wave-number spectrum-function pairs," *Canadian Journal of Physics*, Vol. 46, No. 19, 2133–2153, 1968.

26. Zernov, N. N., "Scattering of waves of the SW range in oblique propagation in the ionosphere," *Radiophysics and Quantum Electronics*, Vol. 23, No. 2, 109–114, 1980.

27. Xu, Z. W. and J. Wu, "On the mutual coherence function and mean arrival time of radio propagation through the turbulent ionosphere," *IEEE Transactions on Antennas and Propagation*, Vol. 56, No. 8, 2622–2629, August 2008.

28. Jandieri, G., Z. Diasamidze, and M. Diasamidze, "Scintillation spectra of scattered electromagnetic waves in turbulent magnetized plasma," *Journal of Basic and Applied Physics*, Vol. 2, 224–234, November 2013.

29. Ning, B., G. Li, and H. Yuan, "Analysis of ionospheric scintillation spectra and TEC in the Chinese low latitude region," *Earth Planets Space*, Vol. 59, 279285, May 2007.

30. Martyn, D. F., "The propagation of medium radio waves in the ionosphere," *Proceedings of the Physical Society*, Vol. 47, No. 2, 323–339, March 1935.